agriculture

MDPI

Article

Multilevel Stability and Load-Transfer Behaviour of a Large-Span Chinese Solar Greenhouse Under Non-Uniform Snow Loading and As-Built Joint Conditions

Zhijie Zheng [1], Changji Zhou [2], Long Zhang [3], Zhaohui Zhang [1], Shuo He [1] and Encai Bao [1,2,*]

[1] School of Civil Engineering, Nanjing Forestry University, Nanjing 210037, China
[2] Key Laboratory of Agricultural Engineering of the Middle and Lower Reaches of the Yangtze River of Ministry of Agriculture and Rural Affairs, Institute of Agricultural Facilities and Equipment, Jiangsu Academy of Agricultural Sciences, Nanjing 210014, China
[3] College of Engineering, Nanjing Agricultural University, Nanjing 210095, China
* Correspondence: baoencai1990@163.com

Abstract

The stability of large-span Chinese solar greenhouses depends not only on snow-load distribution but also on support continuity and the progressive engagement of as-built joints. To distinguish these effects, this study presents a multilevel investigation combining geometrically and materially nonlinear frame analysis, a full-scale sequential hanging-load test with shell-model comparison, and refined solid modelling of design-reference and as-built joints. These three levels are complementary but mechanically uncoupled. Four global cases were analysed: supported-uniform (SU), supported-non-uniform (SN), unsupported-uniform (UU), and unsupported-non-uniform (UN). Their ultimate total vertical loads were 12.336, 11.594, 2.592, and 2.069 kN, respectively. Non-uniform snow reduced the ultimate load by 6.0% for the supported frame and by 20.2% for the unsupported frame, while removal of the intermediate columns reduced the capacity by 79.0% under uniform snow and by 82.2% under non-uniform snow. For the SN case, changing the initial-imperfection amplitude from L/2000 to L/1000 reduced the ultimate load by only 0.285%, indicating that the principal capacity hierarchy was insensitive to the investigated amplitude range. The shell model reproduced the measured strain signs and principal loading trends. At the final 40 kg state, the absolute strain differences ranged from 0.091 to 0.931 με, whereas the sequence-level root mean square errors ranged from 1.289 to 6.361 με, indicating larger path-dependent discrepancies at some intermediate loading stages. The refined as-built joint model indicated progressive closure of the column-top–longitudinal-member gap, with an interpolated contact-onset load of approximately 129.7 N and non-zero normal contact pressure at the next prescribed load of 149.4 N. Under the baseline truncation boundary, the simulated column-reaction share increased to 87.8% at 1000 N; alternative spring boundaries produced shares of 93.9–97.4%, demonstrating that the exact value was boundary-dependent while the progressive engagement mechanism remained consistent. Overall, support continuity dominated the stability capacity of the investigated frame, while as-built gaps and contact conditions governed the delayed mobilisation of the local support path. The local joint results are used for mechanism interpretation and are not propagated into the global ultimate-capacity calculation.

Keywords: Chinese solar greenhouse; nonlinear stability; non-uniform snow; support continuity; as-built joint; load-path redistribution

Check for updates

Academic Editor: Florin Nenciu

Received: 27 August 2026
Revised: 18 October 2026
Accepted: 21 October 2026
Published: 23 October 2026

Copyright: © 2026 by the authors. Licensee MDPI, Basel, Switzerland. This article is an open access article distributed under the terms and conditions of the Creative Commons Attribution (CC BY) license.

1. Introduction

Chinese solar greenhouses are widely used for protected cropping in northern and transitional climatic regions of China. Increasing the structural span improves machinery access and usable production space, but it also lengthens unsupported arch segments and increases reliance on intermediate columns, longitudinal members and assembled joints. Because these structures are lightweight and slender, their response may be governed by geometric nonlinearity and loss of restraint before material yielding occurs [1,2]. Structural assessment therefore needs to consider not only member strength but also whether the roof-to-support load path remains continuous under adverse environmental loading. Stress-state analysis and evaluation of load redistribution have also been applied to mechanically loaded components of agricultural machinery, helping to identify the critical regions governing their structural response and service behaviour [3].

Snow loading is particularly important because its distribution over curved greenhouse roofs is inherently spatially variable. Roof geometry, wind effects and snow sliding may produce strongly non-uniform accumulation patterns [4–6], and previous studies have shown that such distributions can redistribute internal forces and reduce the stability reserve of greenhouse frames [7]. Structural stability is also affected by initial geometric imperfections, member configuration [8,9], column position and lateral restraint [10–12]. These factors are interrelated: the snow distribution determines where structural demand develops, whereas support continuity determines the restraint available to resist that demand. However, previous studies have generally examined snow-load distribution, support arrangement and connection behaviour separately, making it difficult to distinguish their relative contributions within the same structural system.

The stabilising contribution of an intermediate column further depends on whether its column-top connection can effectively transfer roof load into the support. Greenhouse clamp and cross-over connections exhibit semi-rigid behaviour [13–15], while field erection may introduce member eccentricity, bolt-hole clearance, initial gaps and changing contact relationships. Idealised support and connection assumptions can therefore influence finite-element predictions [16]. Computational approaches have similarly been used in agricultural engineering to relate component geometry to the resulting mechanical response and to justify structural or machine-component configurations [17]. Recent as-built reconstruction studies have also demonstrated the importance of representing measured greenhouse geometry in structural analysis [18]. Nevertheless, a global frame model cannot explicitly resolve progressive gap closure, hole bearing and contact activation, whereas an isolated refined joint model cannot independently quantify the global ultimate capacity of the greenhouse. These modelling levels must therefore be interpreted as complementary rather than mechanically coupled.

To address these limitations, the present study adopts a multilevel framework consisting of three complementary analyses. First, a representative-frame model is used to compare the nonlinear stability capacities of supported and unsupported frames under uniform and non-uniform snow loading through a complete (2×2) set of structural cases. Second, a full-scale sequential hanging-load test and a shell-element model are used to evaluate the prediction of local surface-strain response near the front-roof support transition. Third, refined solid models of the design-reference and reconstructed as-built column-top joints are used to investigate gap closure, contact activation and local load redistribution. The three models are not mechanically coupled, and the refined-joint results are used to interpret a possible local mechanism of support engagement rather than to modify the global ultimate-capacity calculation. The objectives are therefore to: (1) quantify the relative effects of snow non-uniformity and support continuity on global stability; (2) assess the ability of the shell model to reproduce the measured local strain response; and (3) clarify how

as-built joint conditions influence the progressive mobilisation of the intermediate-column load-transfer path.

2. Materials and Methods

2.1. Greenhouse Prototype and Structural Configuration

The prototype was a completed Chinese solar greenhouse at a vegetable-production base in Xinba Town, Haizhou District, Lianyungang, Jiangsu Province, China (approximately 119.5° E, 34.5° N). The greenhouse was completed in 2023 and is 80 m long, with a 16 m span and a 6.0 m ridge height. Adjacent arch frames are uniformly arranged at a centre-to-centre spacing of 1.0 m along the longitudinal direction. Columns are installed only beneath the designated main arches, whereas the remaining arches are not directly supported by columns. The main frame comprises a flat-elliptical main arch (80 × 30 × 2 mm), a circular longitudinal tie (25 mm diameter × 2 mm) and circular columns (60 mm diameter × 3 mm). The principal members are Q235 steel with Young's modulus E = 206 GPa, Poisson's ratio ν = 0.30 and yield strength 235 MPa [18]. An ideal elastic–perfectly plastic material model was adopted, consistent with the numerical analyses reported below. The finite-element analyses were performed using ANSYS Mechanical 2022 R2 (ANSYS, Inc., Canonsburg, PA, USA). Strain measurements were conducted using BE120-5AA resistance strain gauges (Ningbo Xiaying Chenyue Electromechanical Equipment Firm, Ningbo, China) connected to a uT7116Y strain measurement instrument (Hubei Zhongheng Electrical Measurement Technology Co., Ltd., Hubei, China).The representative transverse frame and key structural components are shown in Figure 1.

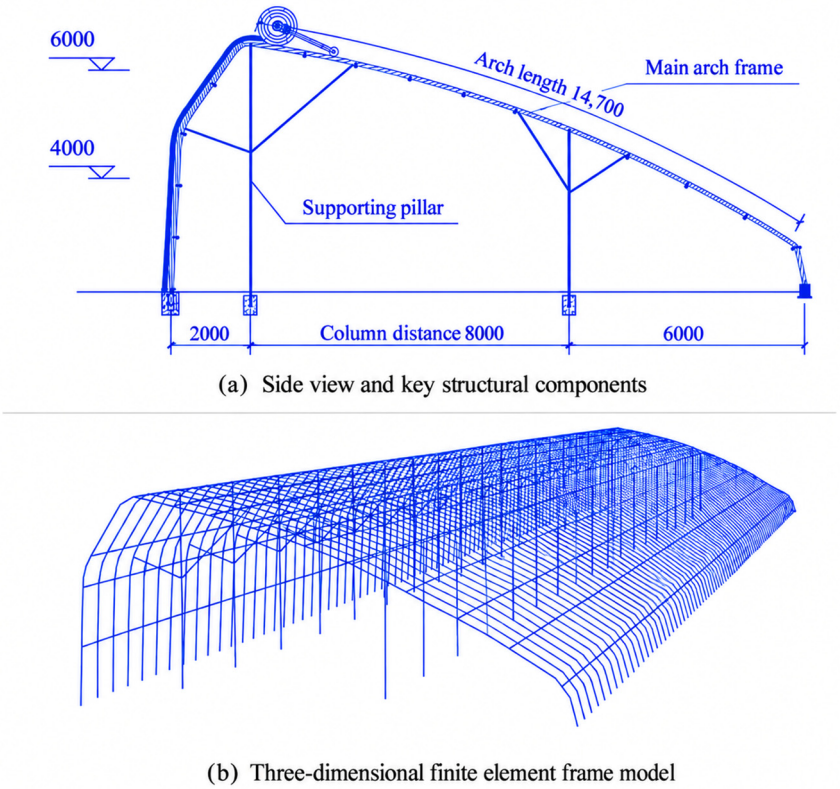


Figure 1. Structural configuration of the investigated 16 m span Chinese solar greenhouse: (**a**) Side view and key structural components; (**b**) three-dimensional structural arrangement used to identify the representative transverse frame.

2.2. Nonlinear Stability Model Under Snow Loading

A representative transverse frame was established in ANSYS Mechanical 2022 R2 (ANSYS, Inc., Canonsburg, PA, USA) using BEAM188 elements to evaluate global buckling and nonlinear ultimate response. A 1 m longitudinal tributary width was assigned, and snow was applied vertically over the horizontal roof projection. In accordance with GB/T 51183–2016 [19], a basic snow pressure s_k = 0.20 kN m^{-2} was adopted for Lianyungang, corresponding to a 20-year return period, and the greenhouse was treated as unheated. The roof snow pressure was calculated as $s(x) = \mu(x)s_k$. For the uniform case, μ = 0.4 was applied over the entire roof projection. For the non-uniform case, μ = 0.4 was retained over the rear-roof region from x = 0 to 2000 mm. Over the front-roof region from x = 2000 to 15,000 mm, μ increased linearly from 0.4 to 2.0 at one-third of the front-roof projected length (x = 6333 mm) and then decreased linearly to zero at x = 15,000 mm. The spatial pattern was kept fixed during nonlinear load amplification.

The global stability analysis was performed using a representative transverse-frame model established with three-dimensional BEAM188 elements. Although BEAM188 provides three-dimensional translational and rotational degrees of freedom, the frame geometry, applied snow load, and evaluated instability response were primarily located within the transverse frame plane. The model therefore represented the in-plane nonlinear stability response of a single transverse frame rather than the complete 80 m long greenhouse or a multi-bay three-dimensional substructure. The three-dimensional structural arrangement shown in Figure 1b was used only to identify the position of the representative frame within the prototype greenhouse.

All column-base nodes were fixed to represent their connections to the concrete foundations, with UX, UY, UZ, ROTX, ROTY, and ROTZ restrained. The main-arch–column connections were modelled as rigid by coupling coincident beam nodes, and no rotational releases were assigned at these joints.The 80 mm major axis of the flat-elliptical main-arch section was oriented approximately normal to the roof centreline so that the larger section dimension resisted the principal in-plane bending action.

The restraint provided by the omitted longitudinal structural system was represented by linear translational springs acting along the global *Z* direction, normal to the plane of the representative transverse frame. Each spring transmitted only translational force along its *Z*-axis and did not transfer bending moments or restrain the rotational degrees of freedom of the connected beam node. The spring stiffness was derived from the equivalent bending restraint of the 25 mm × 2 mm longitudinal tubular member. With E = 206,000 N mm^{-2}, $I = \pi(25^4 - 21^4)/64$ = 9628.2 mm^4, and an effective restraint length Le = 1000 mm, the adopted stiffness was $kz = 3EI/Le^3$ = 5.95 N mm^{-1}. The springs were defined as linear bilateral elements and therefore permitted both tensile and compressive forces along the *Z* direction, although their contribution under the investigated snow-loading condition was predominantly compressive. This treatment represented the equivalent out-of-plane restraint provided by the omitted longitudinal members and did not constitute a rigid arch–tie moment connection or a complete three-dimensional simulation of longitudinal load redistribution.

The self-weight of the steel members was included through gravitational acceleration. The covering film was not explicitly included as either a load-carrying component or an additional dead load, and permanent equipment and other load combinations were also excluded. Accordingly, the reported capacities represent the nonlinear limit loads of the selected transverse frame under the prescribed snow-load patterns and modelling assumptions; they should not be interpreted as the longitudinal or out-of-plane stability capacities of the complete greenhouse. The two prescribed snow-load distributions are shown in Figure 2.

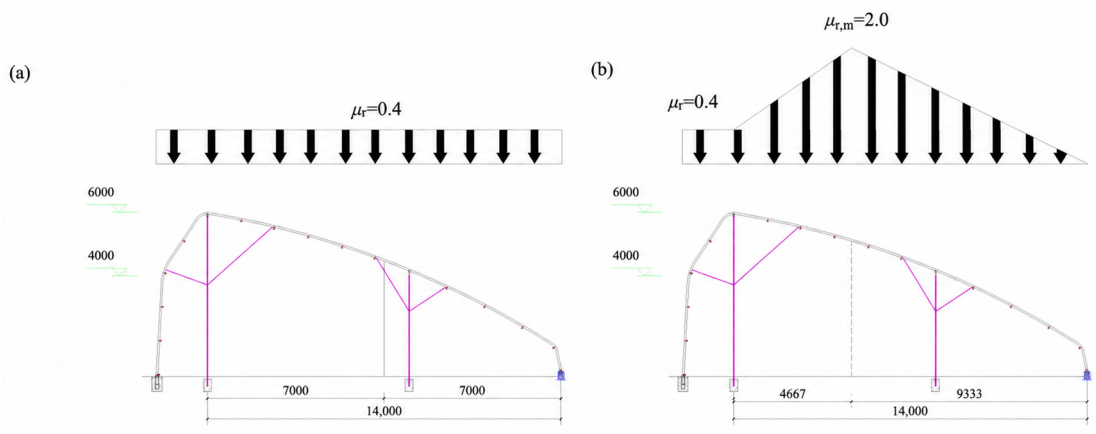


Figure 2. Uniform and non-uniform snow distributions used for the representative-frame stability analysis. Black arrows indicate the applied vertical snow pressure, the coloured lines show the representative frame geometry, and the dashed vertical lines mark the breakpoints of the prescribed snow distribution.

Eigenvalue buckling analysis was first performed, and the first relevant global mode (Figure 3) was used as the shape of the initial geometric imperfection, following the global-imperfection principle in GB 50017-2017 [20]. Because a complete measured imperfection field was unavailable, a common baseline amplitude of L/1500 was adopted with reference to the order of erection tolerances in GB 50205-2020 [21]. For L = 16 m, the maximum imperfection amplitude was 10.7 mm. The imperfect geometry was then analysed with large-deformation effects and the arc-length method. Ultimate capacity was defined as the total vertical load at the limit point. Four global stability cases were analysed by combining the presence or absence of the two intermediate columns with uniform or non-uniform snow loading: supported-uniform (SU), supported-non-uniform (SN), unsupported-uniform (UU), and unsupported-non-uniform (UN). The four cases retained the same member properties, imperfection shape, nonlinear solution settings, and boundary assumptions for the remaining structural components. The L/1500 imperfection amplitude was used as the baseline for the four-case comparison. To evaluate the influence of imperfection magnitude, the SN case was additionally analysed using amplitudes of L/2000 and L/1000, with all other modelling assumptions kept unchanged.

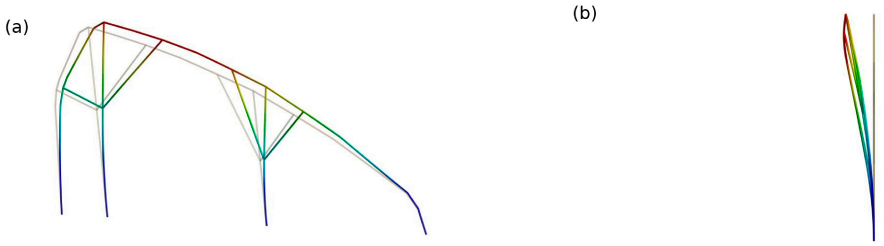


Figure 3. First relevant global buckling mode: (**a**) Front view; (**b**) lateral view. Modal amplitudes are normalised and are used only to define the imperfection shape.The colour variation indicates the normalised modal amplitude and is used only to define the imperfection shape; it does not represent a dimensional displacement magnitude.

2.3. Field Hanging-Load Test and Shell-Model Validation

Nine hanging points (P1–P9) were arranged sequentially along the front-roof main arch. P1 was 2.2 m from the front-roof column base, and the remaining points were spaced at 2.0 m. Standard sandbags were added from P1 to P9 at cumulative levels of 20, 40 and 60 kg per point. Four longitudinal strain gauges (S1–S4) were installed around the front-

roof support transition: S1 was located on the side surface of the column-top region near the arch–column connection, S2 was located on the side surface of the column bottom region 500 mm above the ground, S3 was located on the lower surface of the arch member 500 mm horizontally away from the supporting column, and S4 was located at the mid-span region of the arch member (Figure 4). The test provided local structural responses under known positions and loading sequences; it was not intended to reproduce the code-defined snow distribution. A representative field view of the hanging-load test is shown in Figure 5.

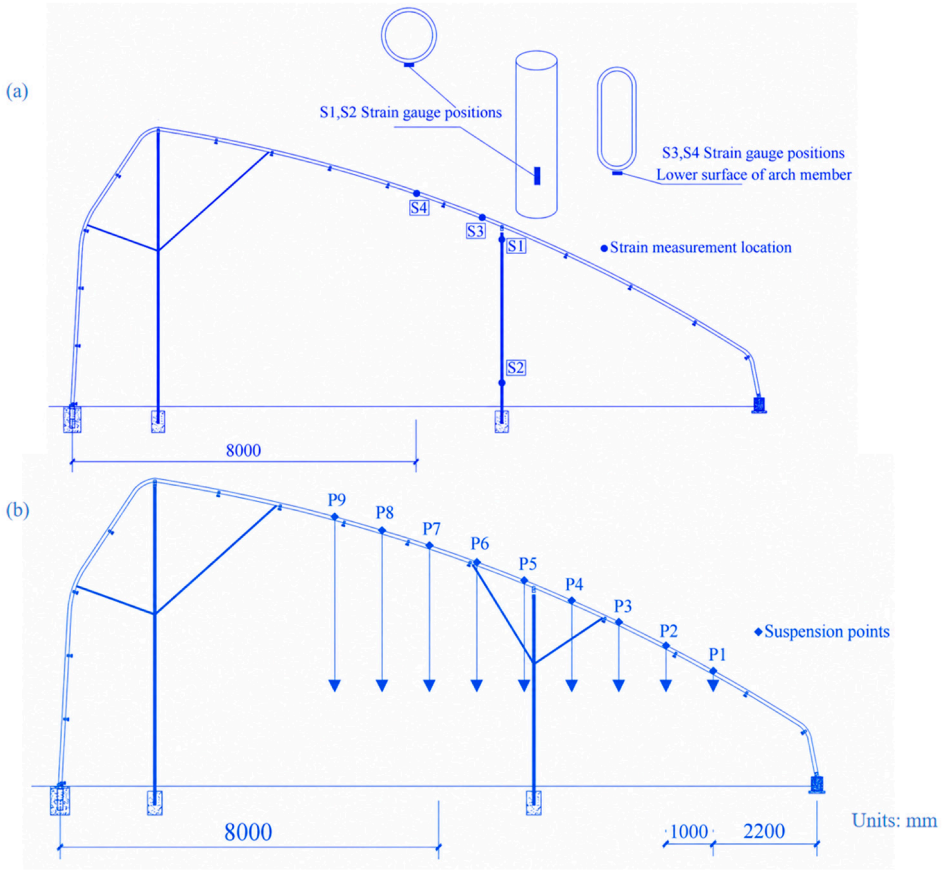


Figure 4. Arrangement of strain gauges and suspension loading points: (**a**) Strain-gauge locations and numerical extraction positions; (**b**) sequential suspension loading points (P1–P9).

An ANSYS shell-element model using mixed quadrilateral and triangular SHELL181 elements reproduced the measured member geometry, wall thicknesses and P1–P9 loading sequence. Vertical forces corresponding to 20 and 40 kg per point (196.2 and 392.4 N) were simulated quantitatively; the 60 kg level (588.6 N) was retained only for qualitative interpretation because some weights later contacted the ground. The hanging-load test was not intended to reproduce the code-defined snow distribution directly. Instead, it provided controlled vertical loading at known positions to evaluate whether the numerical model could accurately reproduce the local strain-transfer behaviour of the greenhouse structure. Therefore, the comparison between the test and simulation should be interpreted as validation of structural response prediction rather than direct validation of snow-load capacity. Local surface longitudinal strain was extracted at the measured gauge positions and orientations. The strain measurements were obtained using BE120-5AA uniaxial foil resistance gauges with a nominal resistance of 120 Ω and a gauge length of 5 mm. The signals were recorded using a 16-channel uT7116Y static strain-acquisition system with a measurement range of ±30,000 με, a resolution of 0.1 με, and a specified error of ±(0.01% of full scale + 0.5 με). The stored readings at all gauges were recorded at inter-

vals of approximately 5–6 s, corresponding to an effective output rate of approximately 0.17–0.20 Hz. After each load increment, the load was held for 5 min to allow the structural response and instrument readings to stabilise. The reading at the end of the 5 min holding period was used as the representative strain for that load level; no moving-average time window was applied. Temperature compensation was provided by an additional gauge bonded to a companion steel tube of the same material and exposed to the same environment. Before loading, channel connectivity and zero stability were checked, the bridge was balanced, and the initial readings were zeroed. All finite-element geometry, material, boundary-condition and load parameters were fixed before comparison with the measured strains; the test data were used for validation and not for model calibration. Measured and simulated strains were paired by gauge, loading sequence and load level. Measured and simulated strains were paired at the same gauge and the same sequential loading step. For gauge i, the absolute error at the final cumulative 40 kg state was calculated as $AE_i = |\varepsilon_i^{\mathrm{sim}} - \varepsilon_i^{\mathrm{exp}}|$. To quantify agreement over the complete loading path, the root mean square error was calculated separately for the nine sequential loading steps of each loading stage as $\mathrm{RMSE}_{i,s} = \sqrt{\frac{1}{n_s}\sum_{j=1}^{n_s}\left(\varepsilon_{i,s,j}^{\mathrm{sim}} - \varepsilon_{i,s,j}^{\mathrm{exp}}\right)^2}$, where s denotes the 20 or 40 kg loading stage and $n_s = 9$. Relative error was not reported because several measured strains at S1 were close to zero. Therefore, AE and stage-specific RMSE were used as the quantitative comparison metrics.



Figure 5. Full-scale greenhouse during the sequential field hanging-load test.

2.4. Refined Design-Reference and As-Built Joint Models

The front-roof main-arch-to-column connection was selected for refined analysis because it is the local transition through which roof load is transferred into the intermediate column and because the adjacent gauges showed clear load-dependent strain evolution. The refined models contained the main arch, clamp, connecting lugs, solid bolts, bolt-hole surfaces, column-top support, column and longitudinal member. The tubular column, main arch and longitudinal member were swept using predominantly higher-order hexahedral SOLID186 elements. Multizone meshing was used for the clamp and column-top support: sweepable subregions were represented by SOLID186 elements, whereas geometrically non-sweepable transition regions were filled locally with SOLID187 tetrahedral elements.

Local refinement was concentrated at bolt holes, lug roots, clamps and contact interfaces. For the 2 mm thick clamp and ear-plate regions, the coarse, medium and fine meshes used two, three and four elements through the thickness, respectively.

The design-reference model aligned the members with their design axes and excluded erection offset and initial gaps (Figure 6). In this reference state, the longitudinal tie did not form an effective vertical bearing path with the column-top support, so load was transferred primarily through the arch–clamp–lug–bolt–column route. The as-built model reproduced the measured geometry of the reconstructed joint. The centreline eccentricity between the main arch and the column was approximately 50 mm. The local initial separation between the column top and the longitudinal member varied from approximately 2 to 3 mm, with a minimum initial gap g_0 of approximately 2 mm. The clamp and the connecting ear plate were both 2 mm thick. The connection used M12 bolts with a nominal shank diameter of 12 mm and bolt holes with a diameter of 13 mm. The resulting diametral clearance was therefore 1.0 mm, corresponding to a nominal single-sided radial clearance of 0.5 mm when the bolt was centred in the hole. These measured geometric characteristics were reproduced directly in the solid model, and the initial separation was retained during contact initialisation so that gap closure and progressive contact activation could develop under external loading. The comparison therefore represents the combined as-built installation state rather than the isolated effect of a single eccentricity parameter.



Figure 6. Design-reference idealised in-plane solid-joint model.The colours are used only to distinguish the joint components and do not represent material differences or result magnitudes.

The two joint models used the same material properties, applied loads and boundary-treatment principles. The column base was fixed in UX, UY and UZ. The cut faces of the two longitudinal-member ends were coupled to remote points. In the baseline model, UX, UY and UZ were restrained at these remote points while rotations remained free. The main-arch cut face was likewise coupled to a remote point, for which UX and UZ were restrained, and UY was released to avoid introducing an artificial vertical support. These remote constraints represent the equivalent restraint exerted by the omitted continuous members at the local-model truncation planes and do not represent actual built-in ends. To evaluate the influence of the longitudinal-member end restraint, two sensitivity models retained the UX and UZ constraints but replaced UY = 0 at both end remote points with vertical Remote Point–Ground springs. For the 25 mm × 2 mm circular tube, E = 206,000 N mm^{-2}, I = $\pi(25^4 - 21^4)/64$ = 9628.2 mm^4, and an effective continuation length L_e = 1000 mm, the adopted translational stiffnesses were $k_1 = 3EI/L_e^3$ = 5.95 N mm^{-1} and $k_2 = 12EI/L_e^3$ = 23.80 N mm^{-1}. End rotations remained free in both spring cases. Bolt pretension was introduced before external loading. The

connection used three M12 bolts with a nominal shank diameter of 12 mm. The property class of the installed bolts was not documented in the available field records and was therefore not inferred from the Q235 grade of the connected members. In the finite-element model, the bolts were assigned the same elastic–perfectly plastic steel model used for the local steel components ($E = 206$ GPa, $\nu = 0.30$ and $f_y = 235$ MPa); consequently, the calculated bolt stresses were used only for relative comparison between the design-reference and as-built configurations and not for a code-based bolt-resistance check. A small assembly pretension of 100 N per bolt was applied in the first load step to establish initial seating of the bolt–clamp system, after which the pretension was locked during external loading. This value was not intended to represent a design pretension for a high-strength friction-grip bolt. Sensitivity cases of 50, 100 and 150 N were analysed with all other model settings unchanged. Bolt-shank/hole and bolt-head/plate interfaces were frictional, and $\mu = 0.20$ was adopted as the uncalibrated baseline value; $\mu = 0.10$ and 0.30 were additionally examined. The measured initial gaps were retained rather than numerically adjusted to close the interfaces. Comparable values have been used in steel-clamp and bolted-joint studies [22–24]. The as-built tie–column-top-support interface could close progressively, while a no-separation condition maintained normal engagement between the lower clamp opening and the tie. The reference load of 74.7 N applied to the refined joint model was derived from the full-span model through a segment-by-segment conversion based on the prescribed non-uniform snow-load distribution coefficients. The local inclination of the corresponding 0.8 m long arch segment varied from approximately 21° to 23°, and a representative inclination of 21° was adopted for the load conversion. With a longitudinal tributary width of 1.0 m, a basic snow pressure of 0.20 kN m^{-2}, and an area-averaged snow-distribution coefficient of 0.50 over this arch segment, the equivalent vertical load was calculated as $P = 0.20 \times 0.50 \times 1.0 \times 0.8 \times \cos 21^\circ = 0.0747$ kN. The corresponding loads calculated using inclination angles of 22° and 23° were 74.2 and 73.6 N, respectively, indicating that the observed variation in local inclination changed the converted load by less than 1.5%.

The eight prescribed load levels were 74.7, 149.4, 224.1, 298.8, 448.1, 597.5, 746.9 and 1000 N, corresponding to approximately 1, 2, 3, 4, 6, 8, 10 and 13.39 times the 74.7 N reference load, respectively. These levels were selected to cover the pre-contact, initial-contact and progressively engaged stages of the reconstructed joint. The as-built model reproduced the measured geometry of the reconstructed joint, as shown in Figure 7.

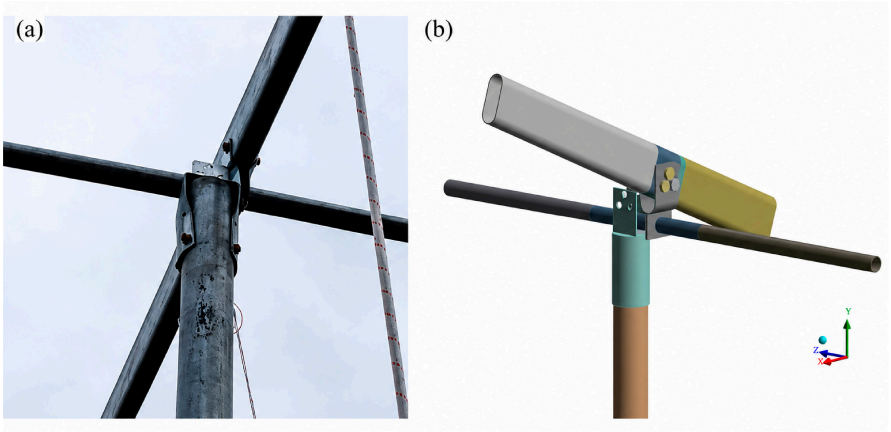


Figure 7. As-built front-roof joint: (**a**) Field configuration; (**b**) refined solid model. The colours in panel (**b**) are used only to distinguish the modelled components and do not represent material properties or analysis-result magnitudes.

2.5. Mesh-Convergence Analysis

Coarse, medium and fine discretisations were checked for the representative-frame, hanging-test shell and refined solid-joint models before the formal analyses. Because the three models address different response scales, convergence was evaluated using model-specific indicators. The complete comparison is summarised in Table 1. The fine mesh was used for the reported stability results, whereas the medium meshes were adopted for the shell and solid-joint analyses after the medium-to-fine changes fell below 2% for the selected response indicators. For the refined joint model, mesh convergence was evaluated at an external load of 597.5 N using three quantities directly related to the investigated mechanism: the column-base vertical reaction F_y, the area-averaged normal contact pressure at the column-top–longitudinal-member interface, and the regional average equivalent stress in the joint control region. The coarse, medium and fine meshes used nominal local element sizes of 6, 4 and 2 mm and two, three and four elements, respectively, through the 2 mm thick clamp and ear-plate regions. The medium-to-fine changes in F_y, average contact pressure and regional average stress were less than 0.01%, less than 0.01% and 2.85%, respectively. The medium mesh was therefore adopted as a balance between contact-response convergence and computational cost. After the overall meshing was completed, the meshes of the solid and shell models are shown in Figure 8 and Figure 9, respectively.

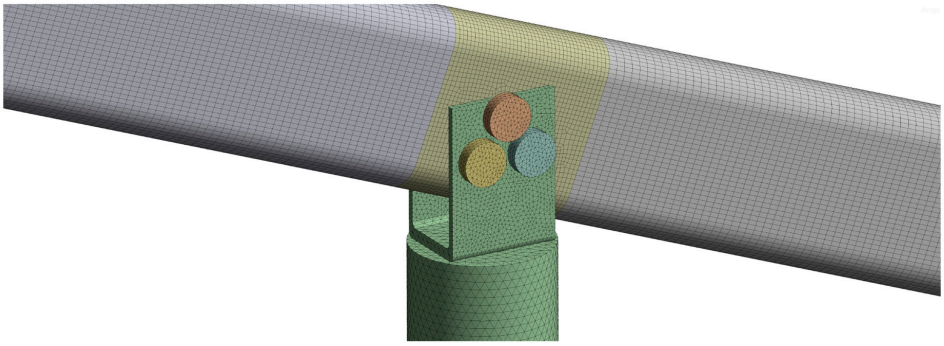


Figure 8. Representative finite-element mesh for the solid model analysis.The colours distinguish different component bodies and mesh regions only; they do not represent analysis-result magnitudes.

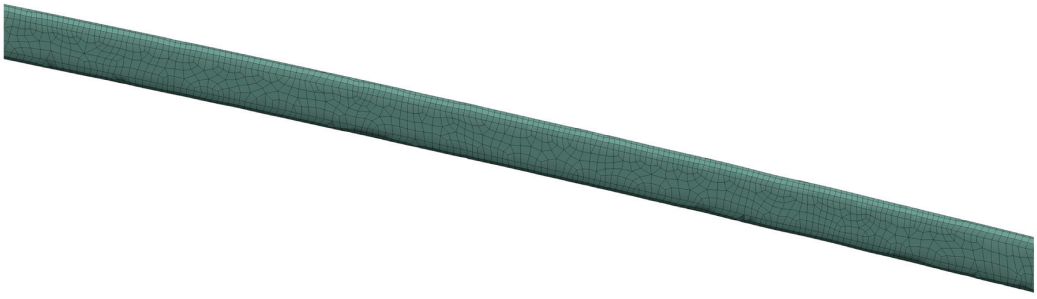


Figure 9. Representative finite-element mesh of the shell-model analysis (mixed quadrilateral and triangular shell elements). Note: Because BEAM188 is a line element, its discretisation is represented by element connectivity rather than surface mesh grids.

Table 1. Combined mesh-convergence results for the three finite-element models.

Model	Mesh	Element Size (mm)	Nodes	Elements	Response 1	Response 2
Frame stability	Coarse	200	619	311	λ_1 = 8.3980	Fu = 12.165 kN
	Medium	100	917	460	8.4038 (0.069%)	12.301 (1.106%)
	Fine	50	1815	909	8.4037 (0.001%)	12.336 (0.284%)

Table 1. *Cont.*

Model	Mesh	Element Size (mm)		Nodes	Elements	Response 1	Response 2
Shell validation	Coarse	200/80		21,364	22,013	u = 142.36 mm	S2 = −48.564 με
	Medium	100/40		38,746	38,694	145.64 (2.25%)	−50.321 (3.492%)
	Fine	50/20		58,778	58,202	146.45 (0.55%)	−51.330 (1.966%)
Solid joint	Mesh	Local size/mm	Wall layers	Nodes	Elements	F_y/N	Mean pressure/MPa
	Coarse	6	2	205,426	33,351	473.74	0.70638
	Medium	4	3	309,365	57,101	476.09	0.33939
	Fine	2	4	346,331	63,203	476.09	0.33950

Note: Values in parentheses are changes relative to the next coarser mesh, calculated using the finer mesh as the denominator. For shell and solid models, element size is given as global/local refinement size. Response 1/2 denote λ_1 and Fu for the frame model, control displacement and S2 strain for the shell model, and control displacement and regional average equivalent stress for the solid model.

3. Results

3.1. Stability Under Non-Uniform Snow and Loss of Column Support

The nonlinear analyses showed that intermediate columns provided substantial restraint to the front-roof arch system. The supported and unsupported configurations exhibited distinctly different deformation patterns, confirming the importance of support continuity in maintaining the global stability reserve. The corresponding deformation patterns of the supported and unsupported configurations are shown in Figure 10 and Figure 11, respectively.

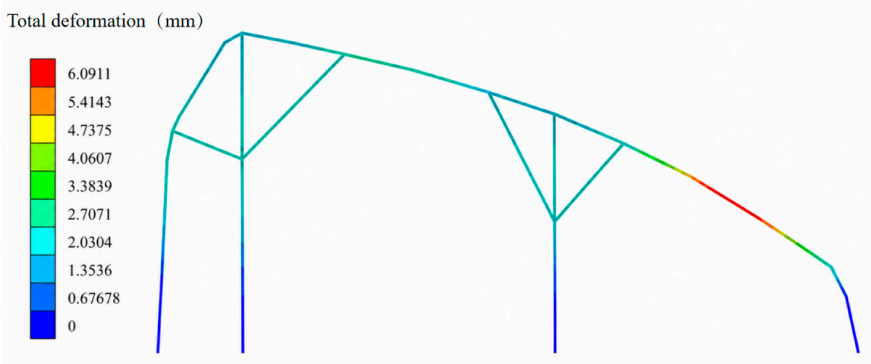


Figure 10. Total deformation of the representative frame with columns under the common reference non-uniform snow load. Values are in mm and do not represent the nonlinear limit point.

Using the baseline initial-imperfection amplitude of (L/1500), the ultimate total vertical loads of the supported-uniform (SU), supported-non-uniform (SN), unsupported-uniform (UU), and unsupported-non-uniform (UN) cases were 12.336, 11.594, 2.592, and 2.069 kN, respectively. For the supported configuration, changing the snow-load distribution from uniform to non-uniform reduced the ultimate load by 6.0%, whereas the corresponding reduction reached 20.2% for the unsupported configuration. Removing the intermediate columns decreased the ultimate load by 79.0% under uniform snow loading and by 82.2% under non-uniform snow loading. These results demonstrate that support continuity was the dominant factor governing the stability capacity of the investigated frame. Moreover, the absence of intermediate-column support substantially increased the relative sensitivity of the frame to non-uniform snow loading.The nonlinear total vertical load–displacement response of the supported-non-uniform case is shown in Figure 12.



Figure 11. Total deformation of the representative frame after removal of the two main columns under the same reference non-uniform snow load. Values are in mm and do not represent the nonlinear limit point.

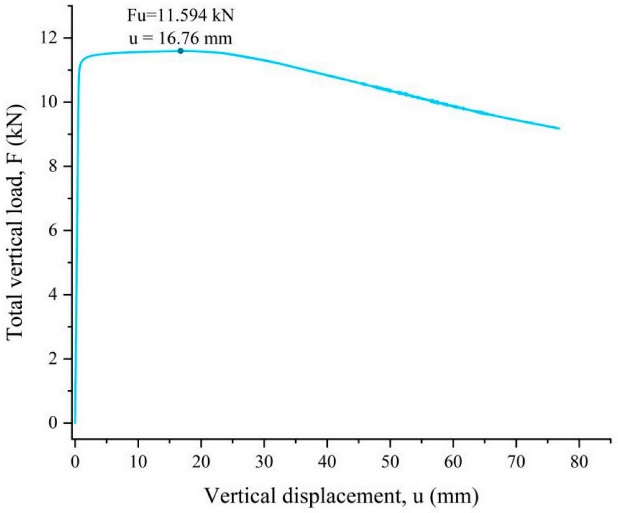


Figure 12. Nonlinear total vertical load–displacement path under non-uniform snow loading; the marked point is the calculated ultimate load.

To evaluate whether the above conclusions were affected by the assumed initial-imperfection amplitude, an imperfection-sensitivity analysis was further conducted for the supported-non-uniform case. Imperfection amplitudes of L/2000, L/1500, and L/1000 produced limit-load factors of 0.722633, 0.721427, and 0.720573, corresponding to ultimate total vertical loads of 11.613, 11.594, and 11.580 kN, respectively. As the imperfection amplitude increased from L/2000 to L/1000, the ultimate load decreased by only 0.285%. Therefore, the predicted capacity exhibited only limited sensitivity to the imperfection amplitude within the investigated range, confirming that the conclusions regarding the dominant influence of support continuity and the adverse effect of non-uniform snow loading were robust with respect to the baseline L/1500 assumption.

3.2. Field Strain Validation

During the controlled 20 and 40 kg stages, S1 remained close to zero, S2 developed compressive strain, S3 accumulated tensile strain, and S4 remained predominantly compressive. The shell model reproduced the strain signs and principal trends at all four gauges, although relatively larger path-dependent discrepancies occurred at some intermediate loading steps for S3 and S4 (Figure 13). At the end of the 40 kg loading sequence, the simulated strains at S1–S4 were −3.861, −51.330, 114.120, and −41.548 με, respectively, compared with the corresponding measured stable values of −2.930, −51.717, 113.745, and

−41.457 με. The resulting absolute differences ranged from 0.091 to 0.931 με, with the maximum absolute difference of 0.931 με occurring at S1 (Table 2).

Table 2. Comparison of measured and simulated strains at the final cumulative 40 kg state and gauge-wise RMSE over each nine-step loading stage.

Gauge	Measured (με)	Simulated (με)	AE (με)	RMSE, 20 kg (με)	RMSE, 40 kg (με)
S1	−2.930	−3.861	0.931	2.326	1.289
S2	−51.717	−51.330	0.387	5.158	3.491
S3	113.745	114.120	0.375	6.024	6.361
S4	−41.457	−41.548	0.091	4.854	5.409

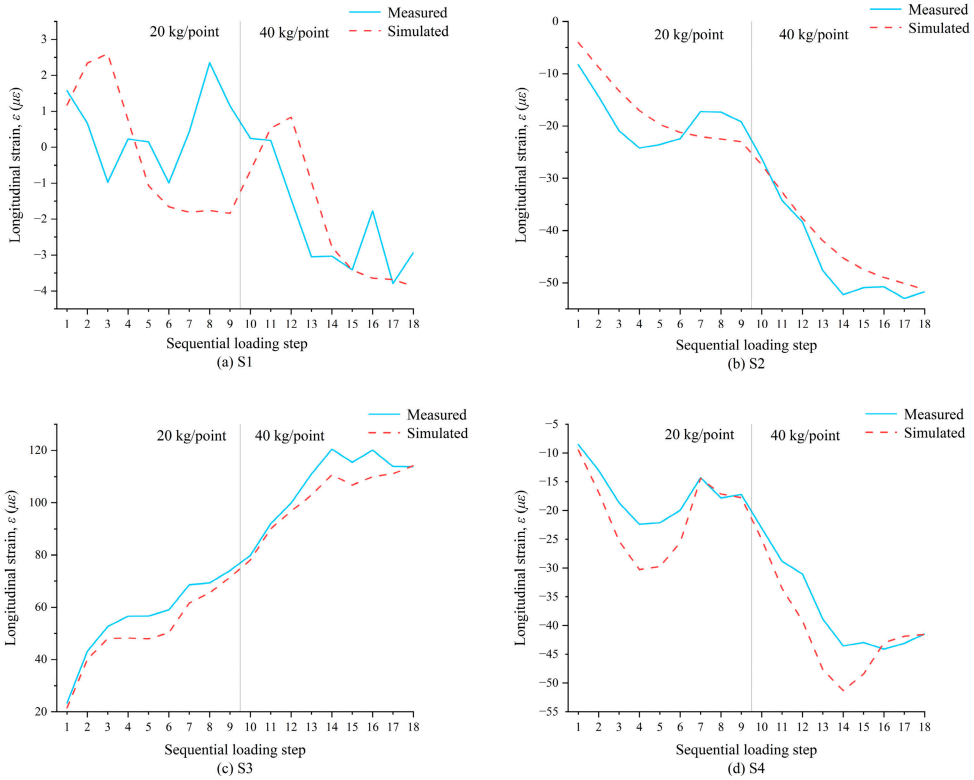


Figure 13. Measured and simulated longitudinal surface strains at S1–S4 during the sequential 20 and 40 kg loading stages.The grey vertical lines separate the 20 kg and 40 kg sequential loading stages.

At the final cumulative 40 kg state, the absolute errors at S1–S4 were 0.931, 0.387, 0.375 and 0.091 με, respectively. These endpoint residuals were all below 1 με; however, they characterise only the final cumulative state and do not describe the agreement over the complete sequential loading path. For the 20 kg loading stage, the RMSE values at S1–S4 were 2.326, 5.158, 6.024 and 4.854 με, respectively, whereas the corresponding values for the 40 kg stage were 1.289, 3.491, 6.361 and 5.409 με. The RMSE decreased from the 20 to the 40 kg stage at S1 and S2, while relatively larger path-dependent discrepancies persisted at S3 and S4. The deviations at intermediate steps are consistent with the sensitivity of the local response to the loading sequence, assembly adjustment and contact or slip mechanisms that were not explicitly represented in the shell model. AE and RMSE are simulation–measurement residual metrics rather than independent estimates of instrument uncertainty. The specified acquisition-system accuracy characterises the measurement channel only and was therefore not used as a substitute for the total uncertainty of the field test. Accordingly, the comparison supports the ability of the shell model to reproduce the measured strain signs, principal trends and final local surface-strain state under the controlled hanging loads,

but it does not constitute direct validation of the global snow-load stability capacity. During the 60 kg stage, the lateral movement of the front-roof column was measured manually using a tape measure and reached approximately 230 mm. After unloading, a residual lateral displacement of approximately 103 mm remained. The observed deformation is shown in Figure 14. Audible structural response, strain fluctuations and partial contact of some hanging weights with the ground were also observed. Because the displacement measurement was not synchronised with an electronic displacement transducer and the effective applied load became uncertain after ground contact, the 60 kg stage was excluded from quantitative validation and was retained only as qualitative evidence of a change in the structural response.



Figure 14. Pronounced lateral deformation of the front-roof frame during the 60 kg loading stage. The maximum lateral displacement of the front-roof column was approximately 230 mm, measured manually with a tape measure relative to a fixed ground reference. After unloading, an approximate residual displacement of 103 mm remained, corresponding to a displacement recovery of approximately 127 mm (55.2%). Owing to the manual measurement method and partial ground contact of some hanging weights, the displacement values at this stage are used only for qualitative interpretation.

3.3. Progressive Activation of the As-Built Support Path

Vertical reaction equilibrium in the as-built solid model was satisfied to within 0.013 N over the eight load levels, confirming that the applied vertical load was transmitted through the defined supports. Load sharing changed strongly as the joint deformed. At 74.7 N, the column-base vertical reaction was essentially zero and the two longitudinal-tie ends each carried about 50% of the load. The column share increased to 19.7% at 149.4 N, 79.7% at 597.5 N and 87.8% at 1000 N, leaving only 12.2% to the two tie ends combined (Figure 15).

The redistribution corresponded to progressive contact activation at the column-top–longitudinal-member interface. The area-averaged normal contact pressure was 0 MPa at 74.7 N and increased to 0.0191, 0.3394 and 0.6370 MPa at 149.4, 597.5 and 1000 N, respectively. This pressure evolution, together with the signed minimum-gap history, shows that effective bearing was absent at the first load level and developed progressively as the joint deformed. The sign of the gap follows the local contact-normal convention; contact onset was therefore identified jointly from the gap evolution, contact status and the appearance of non-zero normal pressure, rather than from the gap sign alone. With further loading, bearing at the column-top support increased and transfer changed from tie-dominated to shared tie–column and finally column-dominated behaviour. A column

may therefore be geometrically present but only become structurally effective as the joint progressively engages. The stabilising contribution of column continuity thus depends on the actual load-transfer path developed within the as-built joint. The numerical activation level near 149.4 N is specific to the reconstructed joint and is not proposed as a general design threshold.

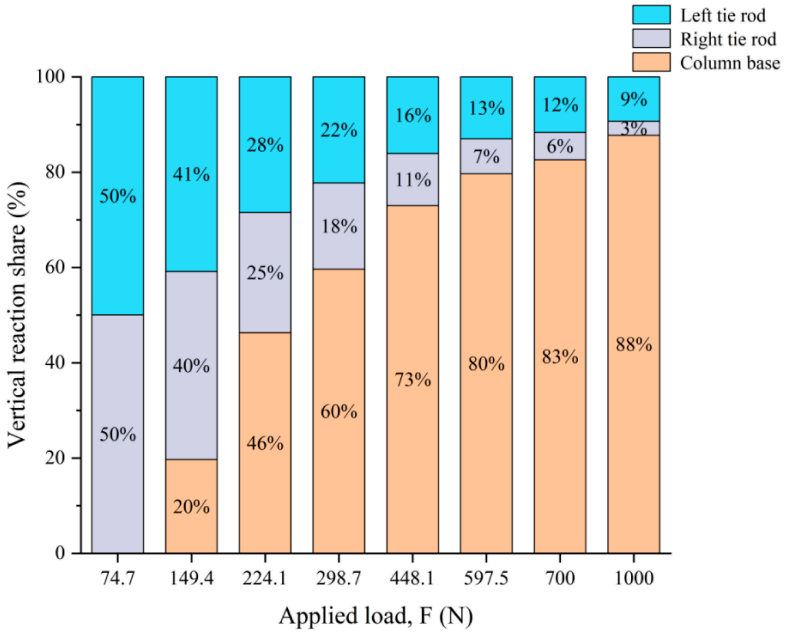


Figure 15. Evolution of vertical reaction shares in the as-built joint during incremental loading.

As the external load increased, the closest-point remaining gap at the column-top–longitudinal-member interface decreased continuously from approximately 2.3 mm at 0 N and reached zero at an interpolated load of approximately 129.7 N, indicating the initial closure of the interface, as shown in Figure 16. At the subsequent prescribed load level of 149.4 N, the development of non-zero normal contact pressure confirmed the establishment of effective bearing and the initial activation of the column-supported load-transfer path. Further loading maintained the interface in contact and progressively increased its contribution to vertical load transfer.

3.4. Design-Reference Versus As-Built Joint Response

The two joint configurations showed different deformation mechanisms over their common load range. In the design-reference joint, the maximum *X*-direction displacement of the column-top support increased gradually from 0.0382 to 0.2325 mm up to 597.5 N, consistent with progressive local bending and rotation. In the as-built model, the clamp mean vertical displacement was already −1.4367 mm at 74.7 N and −2.3133 mm at 149.4 N, then changed only slightly to −2.4173 mm at 597.5 N. At that load, the clamp Y-displacement range was only 0.0450 mm, indicating that most early movement represented positional adjustment of the arch–clamp subsystem relative to the column-top support rather than equivalent local plate bending (Figure 17).

Stress redistribution also differed markedly. In the design-reference joint, Bolt 2 remained the governing bolt; at 597.5 N, its regional average stress was 9.375 MPa. In the as-built joint, Bolt 1 became governing, with an average stress of 4.772 MPa, while Bolts 2 and 3 averaged 3.815 and 3.418 MPa. The common main-arch bolt-hole region increased from 9.292 to 21.341 MPa in the design-reference model but remained around 3.6–4.1 MPa in the as-built model, as load was redirected through newly activated interfaces. The

continuous column segment likewise showed delayed stress development in the as-built state. Figure 18 summarises the stress evolution in the common comparison regions.

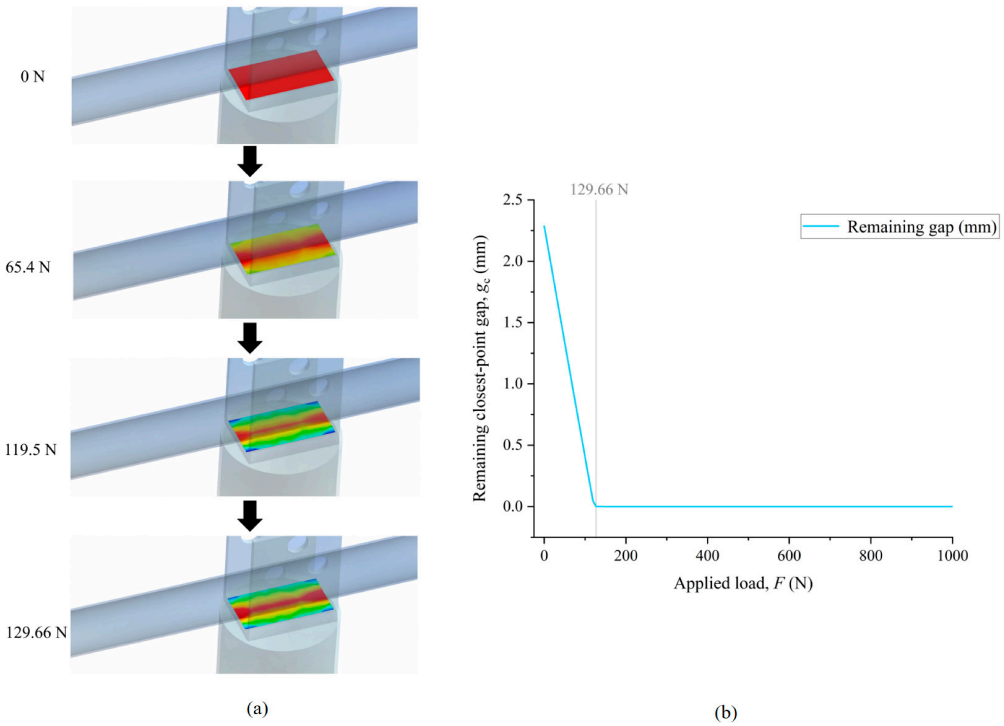


Figure 16. Progressive closure of the column-top–longitudinal-member interface gap under increasing external load: (**a**) Interface-gap distributions at representative load levels; (**b**) closest-point remaining gap versus applied load. The 0 N state corresponds to the condition after the 100 N bolt pretension was applied and locked but before the application of external load. The colour contours in panel (**a**) represent the local interface-gap magnitude in millimetres, while the blue curve in panel (**b**) shows the closest-point remaining gap.

At 1000 N, increasing the friction coefficient from 0.10 to 0.30 changed the maximum and mean contact pressures from 35.445 to 36.073 MPa and from 1.2507 to 1.2626 MPa, respectively, corresponding to differences of 1.77% and 0.95%. In contrast, the maximum and mean slips decreased from 0.050363 to 0.027349 mm and from 0.0019814 to 0.0010501 mm, corresponding to reductions of 45.70% and 47.00%. The normal contact-pressure response and the principal load-transfer interpretation were therefore relatively insensitive to this friction range, whereas the local slip response remained friction-sensitive. The baseline value $\mu = 0.20$ should be regarded as an intermediate, uncalibrated modelling assumption.

Changing the bolt assembly pretension among 50, 100 and 150 N produced maximum spreads of only 0.08%, 0.33%, 0.21% and 0.04% in the column reaction, maximum contact pressure, mean contact pressure and signed-gap metric, respectively, over the complete load history. The first effective-contact stage was also unchanged. Thus, within the investigated small-preload range, the assumed 100 N seating pretension did not materially alter the progressive contact and load-transfer mechanism.

At 1000 N, the column-base vertical reaction share was 87.8% under the baseline remote-displacement boundary condition. When the vertical constraints at the two longitudinal-member remote points were replaced by springs, the share increased to 97.4% for $k = 5.95$ N mm^{-1} and 93.9% for $k = 23.80$ N mm^{-1}. The precise reaction share and activation level are therefore sensitive to the representation of the omitted surrounding structure. Nevertheless, all three boundary representations showed progressive engagement of the column path at higher loads. Accordingly, the value of 87.8% is reported only as

the result for the baseline boundary condition and is not treated as a universal load-sharing ratio.The bolt numbering adopted in this comparison is shown in Figure 19.

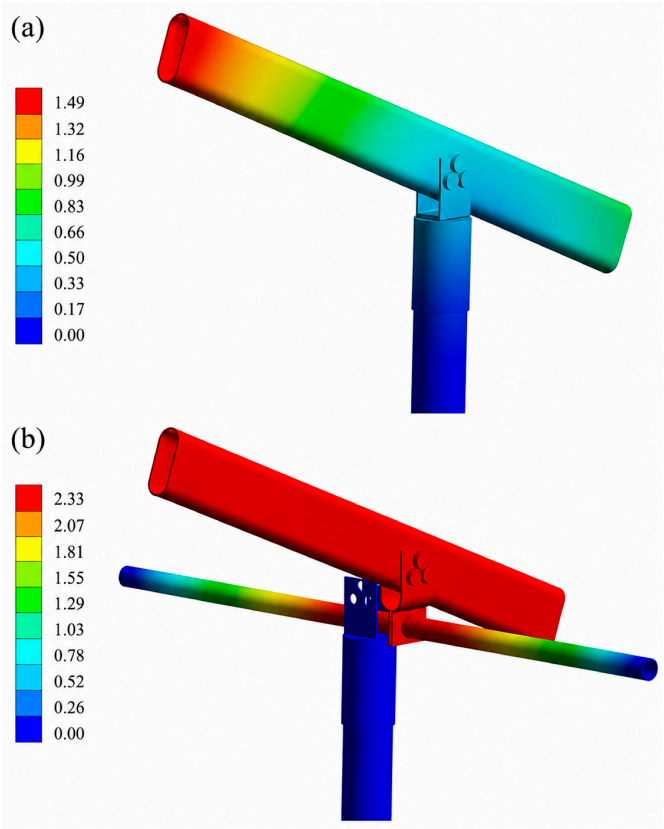


Figure 17. Representative displacement contours of the two joint configurations at an applied load of 597.5 N: (**a**) Displacement of the column-top support in the design-reference joint; (**b**) displacement of the arch–clamp assembly in the as-built joint. Owing to the different spatial arrangements and governing deformation directions of the two configurations, independent displacement components and colour scales are used. The contours are presented only to illustrate their respective deformation modes and are not intended for direct comparison of displacement magnitudes.

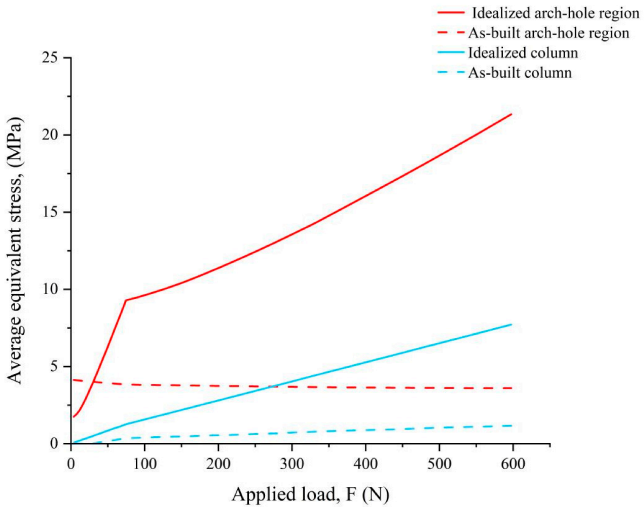


Figure 18. Regional average equivalent stress versus applied external vertical load for the common bolt-hole and column comparison regions in the design-reference and as-built joint models. The 0 N state corresponds to the condition after the 100 N pretension had been applied to each bolt and locked, but before the external vertical load was applied; therefore, the non-zero initial stresses result from bolt pretension and joint seating.

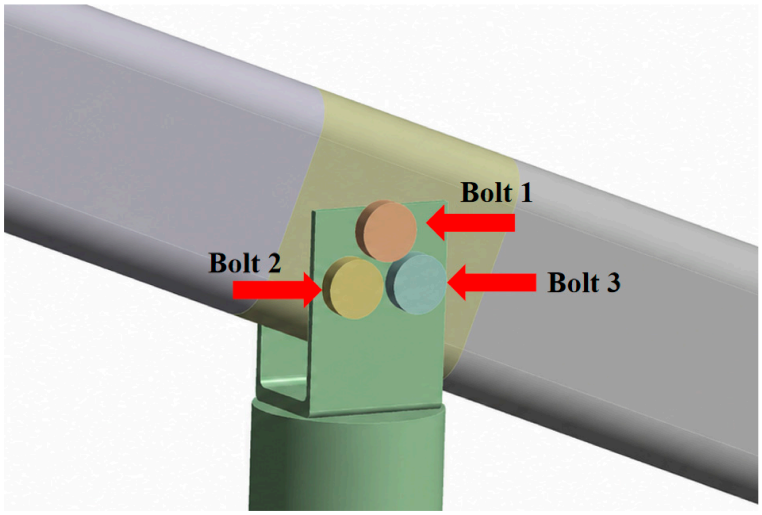


Figure 19. Identification of the three bolts in the refined joint model.

4. Discussion

The frame-scale results establish a clear hierarchy between snow-load distribution and support continuity. Changing from uniform to non-uniform snow reduced the ultimate load by 6.0% for the supported frame and by 20.2% after removal of the two intermediate columns, consistent with previous studies showing that asymmetric snow disturbs coordinated arch action and accelerates instability [4,6,8]. By comparison, removal of the columns reduced the ultimate load by 79.0% under uniform snow and by 82.2% under non-uniform snow. Support continuity was therefore the dominant control for this 16 m prototype, and its loss also amplified the relative adverse effect of snow non-uniformity. The imperfection-sensitivity analysis yielded only a 0.285% reduction in the SN ultimate load as the amplitude increased from L/2000 to L/1000, indicating that this hierarchy was not governed by the baseline L/1500 assumption. This does not make snow non-uniformity secondary in design; rather, it shows that its effect develops within a system whose stability reserve is strongly conditioned by whether the intermediate support path remains available.

The field and joint results explain how that support path is mobilised. The shell model reproduced the final 40 kg strain state with a maximum absolute error of 0.931 με, while larger intermediate discrepancies at S3 and S4 and the qualitative 60 kg response indicated increasing path dependence that a member-level shell model cannot resolve. Under the baseline local boundary condition, the column share of vertical load increased from approximately 0% at 74.7 N to 87.8% at 1000 N as the initial gap closed and contact developed. The preload and friction studies indicated that this progressive normal load-transfer mechanism was not controlled by the assumed 50–150 N assembly pretension or by the investigated $\mu = 0.10$–0.30 friction range, although local slip was friction-sensitive. By contrast, replacing the longitudinal-member end constraints with finite springs changed the 1000 N column share to 93.9–97.4%. The precise load-sharing ratio and contact-onset level are therefore conditional on the truncated-boundary representation, whereas the occurrence of progressive column-path engagement was reproduced by all investigated boundary cases. These local results explain a possible joint-scale mechanism but are not numerically propagated into the global ultimate-capacity calculation because the global and local models are not coupled. Previous greenhouse studies have demonstrated the importance of semi-rigid clamp behaviour [12–14]; the present results extend that understanding by showing that an as-built joint may also change the sequence and location of load-path activation. The change in the bolt exhibiting the highest regional average equivalent stress

from Bolt 2 to Bolt 1 suggests that the installation state redistributed the local numerical stress demand.

For engineering practice, the results point to three linked inspection priorities: asymmetric snow accumulation on the long front roof, continuity and alignment of the intermediate columns, and the actual relative position of the arch, column-top support and longitudinal tie. Pronounced gaps, eccentricity, poorly seated contact interfaces and abnormal lateral column movement should be treated as potential load-path deficiencies rather than cosmetic erection deviations. The reported loads, displacements and activation levels are case-specific and are not proposed as universal acceptance limits; their value is to identify the mechanisms that should be checked in large-span protected-cropping structures and to show why a nominally present support may not provide its full stabilising effect until the joint is effectively engaged.

Although the numerical values of capacity, displacement and activation load are specific to the investigated greenhouse, the identified mechanism of support-path activation is applicable to other assembled greenhouse structures with similar semi-rigid connection characteristics.

5. Limitations

The study concerns one 16 m span greenhouse and one instrumented front-roof region. The field test used single-surface strain gauges without synchronised global displacement, joint rotation or contact-slip measurements; consequently, the 20 and 40 kg stages validate local longitudinal surface strain rather than global stability. The 60 kg stage is qualitative because partial ground contact of the hanging weights made the effective input load uncertain. The calculated stability capacities are also conditional on the common L/1500 imperfection because a complete measured as-built imperfection field was unavailable.

The design-reference and as-built joint models differ simultaneously in eccentricity, longitudinal-member participation, initial gaps and contact relationships; consequently, their comparison identifies the combined installation-state effect rather than the isolated contribution of each geometric feature. The actual bolt property class and installed pretension were not documented, and $\mu = 0.20$ was not calibrated for the steel surfaces. Although the 50–150 N pretension and $\mu = 0.10$–0.30 friction studies bound these modelling assumptions, the local slip response remained friction-sensitive. The measured initial gap g_0 was reproduced directly rather than varied parametrically, so the calculated contact-onset load is specific to the reconstructed 2–3 mm gap geometry. The boundary-condition study further showed that the precise reaction share depends on the equivalent restraint assigned at the model truncation planes. Finally, the global and refined models were not coupled; the joint results are therefore used to interpret the load-transfer mechanism rather than to modify the predicted global ultimate capacity. Future work should use measured bolt properties and installation torque, surface-friction tests, a parametric range of erection gaps, and a larger substructure or experimentally calibrated joint law. Future work should combine measured as-built geometry, interface-friction and bolt-slip tests, intermediate joint configurations, and synchronised displacement or digital image correlation measurements to isolate these parameters and incorporate experimentally calibrated nonlinear joint relations into the frame model.

6. Conclusions

This study investigated the stability and load-transfer behaviour of a 16 m span Chinese solar greenhouse through nonlinear frame analysis, a full-scale sequential hanging-load test, shell-model strain comparison and refined solid-joint simulations. The global, experimental and local numerical analyses represent complementary but mechanically

uncoupled levels. Accordingly, the refined-joint results are used to interpret the mechanism of intermediate-column engagement and are not numerically propagated into the global ultimate-capacity calculation. The principal conclusions are as follows:

1. For the investigated greenhouse, support continuity had a greater influence on global stability capacity than the change from uniform to non-uniform snow loading. The ultimate total vertical loads of the supported-uniform, supported-non-uniform, unsupported-uniform and unsupported-non-uniform cases were 12.336, 11.594, 2.592 and 2.069 kN, respectively. Non-uniform snow reduced the ultimate load by 6.0% for the supported frame and by 20.2% for the unsupported frame, whereas removal of the two intermediate columns reduced the capacity by 79.0% under uniform snow and by 82.2% under non-uniform snow. For the supported-non-uniform case, increasing the initial-imperfection amplitude from (L/2000) to (L/1000) reduced the ultimate load by only 0.285%, indicating that the four-case comparison was insensitive to the investigated imperfection-amplitude range.
2. The shell model reproduced the signs and principal trends of the measured local surface strains during the controlled 20 and 40 kg loading stages. At the final 40 kg state, the maximum absolute difference between the measured and simulated strains at S1–S4 was 0.931 με. Considering the specified measurement accuracy and the absence of synchronised displacement and joint-slip measurements, this agreement should be interpreted as validation of the local strain-transfer response rather than validation of global buckling capacity. The 60 kg stage was retained only for qualitative interpretation because partial ground contact of the hanging weights made the effective applied load uncertain.
3. The reconstructed as-built joint exhibited progressive activation of the intermediate-column load-transfer path. The closest-point gap decreased from approximately 2.3 mm at zero external load and reached zero at an interpolated load of approximately 129.7 N. Non-zero normal contact pressure subsequently developed at the prescribed 149.4 N stage. Under the baseline remote-displacement boundary condition, the column share of the vertical load increased from approximately 0% at 74.7 N to 87.8% at 1000 N. Replacing the longitudinal-member vertical restraints with finite springs changed the corresponding share to 93.9–97.4%. The precise load-sharing value is therefore dependent on the representation of the truncated boundaries, although progressive high-load engagement of the column path occurred in all three boundary cases.
4. The design-reference and as-built joint models exhibited different local stress-transfer patterns. The bolt with the highest regional average equivalent stress changed from Bolt 2 in the design-reference model to Bolt 1 in the as-built model. This comparison identifies a change in the numerically stress-controlling location and should not be interpreted as a code-based bolt-resistance assessment. Because the two models differ simultaneously in eccentricity, initial gap, longitudinal-member participation and contact configuration, the observed differences represent a combined installation-state effect rather than the isolated influence of a single geometric parameter. Within the investigated ranges, changing the bolt seating pretension from 50 to 150 N had little influence on the principal contact response, whereas increasing the friction coefficient from 0.10 to 0.30 had a limited effect on normal contact pressure but substantially reduced local slip.
5. The results suggest that support continuity should be assessed as an effective load-transfer condition rather than solely from the geometric presence of an intermediate column. Winter inspection and construction quality control should therefore focus on asymmetric snow accumulation, column alignment, arch-to-column eccentricity,

excessive gaps, bolt seating and effective contact between the longitudinal member and the column-top support. The numerical loads and contact-activation levels reported in this study are specific to the investigated greenhouse and should not be treated as universal design or acceptance thresholds.

Author Contributions: Conceptualization, Z.Z. (Zhijie Zheng); methodology, Z.Z. (Zhijie Zheng) and C.Z.; investigation, Z.Z. (Zhijie Zheng), L.Z. and S.H.; formal analysis, Z.Z. (Zhijie Zheng); validation, C.Z.; resources, C.Z. and E.B.; data curation, L.Z. and S.H.; visualization, S.H.; supervision, C.Z. and E.B.; project administration, E.B.; funding acquisition, E.B.; writing—original draft preparation, Z.Z. (Zhijie Zheng); writing—review and editing, Z.Z. (Zhijie Zheng), C.Z., L.Z., Z.Z. (Zhaohui Zhang), S.H. and E.B. All authors have read and agreed to the published version of the manuscript.

Funding: This research was funded by the Jiangsu Provincial Basic Research Program Natural Science Foundation, grant number BK20241174.

Data Availability Statement: The raw data supporting the conclusions of this article will be made available by the authors on request.

Acknowledgments: The authors gratefully acknowledge the staff of Chuangjing Agricultural Equipment Group for providing access to the greenhouse and assistance during the field hanging-load tests. The authors reviewed and edited all output and take full responsibility for the content of this publication.

Conflicts of Interest: The authors declare that they have no known competing financial interests or personal relationships that could have appeared to influence the work reported in this paper.

References

1. Li, J.M. Development of the protected vegetable industry (III): Current situation, problems and suggestions for China's protected vegetable structures. *China Veg.* **2023**, *11*, 1–8. (In Chinese) [CrossRef]
2. Briassoulis, D.; Dougka, Y.; Dimakogianni, D.; Vayas, I. Analysis of the collapse of a greenhouse with vaulted roof. *Biosyst. Eng.* **2016**, *151*, 495–509. [CrossRef]
3. Veselovsky, A.; Troyanovskaya, I.; Voinash, S.; Malikov, V.; Zagidullin, R.; Sabitov, L. Features of wear of gears of agricultural machinery. *Acta Technol. Agric.* **2023**, *26*, 207–214. [CrossRef]
4. Wang, C.; Jiang, Y.; Bai, Y.; Wang, T. Numerical study on static properties and failure mechanisms of landing assembled Chinese solar greenhouses. *Comput. Electron. Agric.* **2021**, *188*, 106347. [CrossRef]
5. Choi, Y.B.; Kim, R.W.; Lee, I.B. Numerical analysis of snow distribution on greenhouse roofs using CFD–DEM coupling method. *Biosyst. Eng.* **2024**, *237*, 196–213. [CrossRef]
6. Sun, X.; Zou, J.; Wu, Y.; Li, Y. Investigation of effects of repose angle and critical sliding angle of snow on curved roofs. *J. Wind Eng. Ind. Aerodyn.* **2022**, *227*, 105071. [CrossRef]
7. Li, M.; Wei, X.; Zhao, Q.; Wang, L. Numerical simulation of structural performance in a single-tube frame for 12 m-span Chinese solar greenhouses subjected to snow loads. *Agronomy* **2024**, *14*, 1122. [CrossRef]
8. Wang, C.; Wu, H.; Jiang, Y.; Bai, Y.; Wang, T. Stability analysis of landing assembled Chinese solar greenhouses with discrete lateral braces under snow loads. *Biosyst. Eng.* **2023**, *233*, 168–180. [CrossRef]
9. Wang, C.; Shen, J.; Jiang, Y.; Zhu, L. Failure mechanisms and reinforcement of pipe-framed solar greenhouses under snow loads. *Sci. Rep.* **2025**, *15*, 16403. [CrossRef] [PubMed]
10. Liu, X.; Li, Z.; Zhang, L.; Liu, Y.; Li, Y.; Li, T. Effect of single tube sections on the structural safety of Chinese solar greenhouse skeletons. *Sci. Rep.* **2021**, *11*, 19307. [CrossRef] [PubMed]
11. Ren, J.; Wang, J.; Guo, S.; Li, X.; Zheng, K.; Zhao, Z. Finite element analysis of the static properties and stability of a large-span plastic greenhouse. *Comput. Electron. Agric.* **2019**, *165*, 104957. [CrossRef]
12. Wang, C.; Xu, Z.; Jiang, Y.; Wang, T. Numerical analysis of static and dynamic characteristics of large-span pipe-framed plastic greenhouses. *Biosyst. Eng.* **2023**, *232*, 67–80. [CrossRef]
13. Lee, J.Y.; Ryu, H.R. Structural analysis of pipe-framed greenhouses using interface elements for cross-over connections. *Eng. Struct.* **2022**, *266*, 114504. [CrossRef]
14. Lee, S.; Lee, J.H.; Seo, B.H.; Kim, D.S.; Kim, D.; Jo, Y.; Choi, W. Stiffness evaluation of semi-rigid connection using steel clamps in plastic greenhouse structure. *Biosyst. Eng.* **2025**, *250*, 15–27. [CrossRef]

15. Seo, B.H.; Lee, S.; Kim, D.K.; Lee, J.H.; Kim, D.S.; Kim, D.W.; Jo, Y.; Choi, W. Structural safety assessment procedure of plastic single-span greenhouses considering semi-rigid clamp joints. *Results Eng.* **2025**, *25*, 104106. [CrossRef]
16. Ha, T.; Kim, J.; Cho, B.H.; Kim, D.J.; Jung, J.E.; Shin, S.H.; Kim, H. Finite element model updating of multi-span greenhouses based on ambient vibration measurements. *Biosyst. Eng.* **2017**, *161*, 145–156. [CrossRef]
17. Semenenko, I.I.; Dzjasheev, A.M.S.; Tikhonov, E.A.; Orekhovskaya, A.A.; Mukhametshin, I.S.; Mirzoeva, M.R. Justification of the flat shaft profile using variation calculation methods. *IOP Conf. Ser. Earth Environ. Sci.* **2022**, *981*, 042047. [CrossRef]
18. *GB/T 700-2006*; Carbon Structural Steels. Standardization Administration of China: Beijing, China, 2006. (In Chinese)
19. *GB/T 51183-2016*; Code for Design Load of Horticultural Greenhouse Structures. China Planning Press: Beijing, China, 2016. (In Chinese)
20. *GB 50017-2017*; Standard for Design of Steel Structures. China Architecture & Building Press: Beijing, China, 2017. (In Chinese)
21. *GB 50205-2020*; Standard for Acceptance of Construction Quality of Steel Structures. Ministry of Housing and Urban-Rural Development of the People's Republic of China: Beijing, China, 2020. (In Chinese)
22. Cavalheiro, F.N.; Cabaleiro, M.; Conde, B.; Cruz, Y. Elastic Structural Assessment of Clamp-Based Steel Beam-to-Column Connections for Reusable Steel Systems. *Appl. Sci.* **2025**, *15*, 5398. [CrossRef]
23. Obkircher, D.; Costas, M.; Langseth, M.; Clausen, A.H. Quasi-static and dynamic shear-out resistance in a steel fin-plate connection: An experimental and numerical investigation. *Int. J. Impact Eng.* **2024**, *192*, 105012. [CrossRef]
24. Collini, L.; Garziera, R.; Corvi, A.; Cantarelli, G. Slip strength of COR-TEN and Zn-coated steel preloaded bolted joints. *Results Eng.* **2024**, *22*, 102009. [CrossRef]

Disclaimer/Publisher's Note: The statements, opinions and data contained in all publications are solely those of the individual author(s) and contributor(s) and not of MDPI and/or the editor(s). MDPI and/or the editor(s) disclaim responsibility for any injury to people or property resulting from any ideas, methods, instructions or products referred to in the content.